The frictional strength and stability of spatially heterogeneous fault gouges

Job P.B. Arts [*], André R. Niemeijer, Martyn R. Drury, Ernst Willingshofer, Liviu C. Matenco

Department of Earth Sciences, Utrecht University, The Netherlands

ARTICLE INFO

ABSTRACT

Along-fault lithological heterogeneity is observed in all fault zones that cross-cut compositional layering. Numerical modelling studies on fault rupture nucleation, propagation and arrest often assume that the fault mechanical behaviour is governed by either the rheologically weak phase or by a homogeneous gouge mixture of juxtaposing lithologies. However, the effects of spatial heterogeneity on fault gouge composition and hence its frictional behaviour are less known. In this study, we simulate a mixture of mechanically contrasting rheologies of claystones and sandstones in fault gouges by using lithologies available in the well-known Groningen gas field stratigraphy (Ten Boer and Slochteren members, respectively). Friction experiments were performed in a rotary shear configuration to accommodate the large displacements required to study mixing and clay smearing in faults with large offsets. A velocity stepping procedure was conducted to quantify the rate-dependence of friction and its evolution with displacement. A spatial heterogeneity was introduced by segmentation of the simulated gouge in claystone and sandstone patches.

In contrast to previous studies, we show that Slochteren sandstone gouges can exhibit velocity-weakening behaviour related to strain-localization in a principal slip zone with reduced grain size. Our experiments on segmented gouges show displacement-dependent changes in the sliding friction and its rate-dependence. Clay smearing and shear localization on foliation planes cause weakening of the gouge and a shift from velocity-weakening to velocity-strengthening behaviour. Progressive shearing leads to juxtaposition of sandstone segments that are separated only by a thin clay smear. We propose that the associated increase in friction is caused by lithology mixing at the interfaces between the clay smear and the bulk Slochteren sandstone gouge, and by the disruption of continuous Y-shears. Progressive shearing does not lead to a decrease in the rate-sensitivity parameter (*a-b*). This observation suggests that shearing remains localized on phyllosilicate foliations, possibly accommodated by the increased width of the principal slip zone (PSZ) with displacement.

Our results show that fault friction and its rate-dependence are not simply governed by the weakest lithology along a fault plane, nor that they can be simply represented by a homogeneous mixture of the juxtaposing lithologies. Detailed knowledge of the stratigraphic layering in combination with the fault offset is required to predict the macroscopic frictional behaviour of heterogeneous fault gouges.

1. Introduction

Large offset faults are complex shear zones that show heterogeneity at various spatial scales (Caine et al., 1996; Collettini et al., 2009; Fagereng and Sibson, 2010; Tesei et al., 2014; Torabi et al., 2020). Such shear zones consist of a core, accommodating most strain, and a less deformed damage zone (e.g. Faulkner et al., 2010; Caine et al., 1996; Torabi et al., 2020). The fault core may comprise breccias, cataclasites, fault gouges and clay smears as well as lenses of rigid material surrounded by a weaker foliation of phyllosilicates (Collettini et al., 2009; Faulkner et al., 2003, Giorgetti et al., 2015). Once a core has formed, deformation is localised in one or multiple principal slip zones (PSZ) within a fault gouge composed of finer grained material produced by frictional wear of rocks traversed by the fault (Chester and Chester, 1998; Collettini et al., 2009; Hunfeld et al., 2017; Sibson, 1986). The fault slip behaviour (seismic slip versus stable aseismic sliding) is controlled by the composition and microstructural state of the fault gouge.

Laboratory studies on natural and simulated fault gouges of various rock types show typical friction coefficients (μ) ranging between 0.6 and 0.85 (e.g. Byerlee, 1978; Dieterich, 1972; Scholz, 2019). The presence of weak phyllosilicate minerals can reduce the frictional strength to values

of μ < 0.5 (Byerlee, 1978; Collettini et al., 2009; Collettini et al., 2019; Ikari et al., 2011; Tembe et al., 2010). These studies also show that the rate-dependence of friction and hence the fault stability in a rate-and-state friction (RSF) framework of fault mechanics depends on the fault gouge composition (Dieterich, 1978, 1979; Marone, 1998; Ruina, 1983). Frictionally weak gouges (μ < 0.5) typically exhibit velocity-strengthening behaviour, whereas strong gouges exhibit both velocity-strengthening and -weakening behaviour (e.g. Ikari et al., 2011). Faults that truncate both frictionally strong and weak lithologies may produce a variety of fault gouge compositions, depending on the along-fault lithology distribution and amount of fault displacement. The effect of along-fault heterogeneity on the evolution of fault gouge composition and structure is critical for predicting the fault mechanical behaviour but is still poorly understood.

Existing experimental studies have partly addressed some of the spatial heterogeneity effects on the frictional behaviour of simulated gouges. In multi-phase fault gouges, significant weakening occurs when localization of deformation occurs in a rheologically weak phase. In homogeneously mixed gouges, the transition from granular flow to localised shearing only occurs when the weak phase forms a continuous layer with a critical thickness (Giorgetti et al., 2015; Ikari et al., 2011; Tembe et al., 2010). This observation is confirmed by experiments with spatially heterogeneous gouges with predefined layering parallel to the shear direction (Niemeijer et al., 2010; Smeraglia et al., 2017). These studies only account for fault-parallel heterogeneity and do not consider how such structures evolve from initial fault perpendicular layering. Studies that do consider such along-fault compositional heterogeneity (Bedford et al., 2022; Buijze et al., 2020) only allow for small displacements (<25 mm) and are, therefore, representative only for the initial slip along mechanically contrasting layers.

In terms of natural analogues, one of the best available case studies is the Groningen gas field in the Netherlands due to the advanced state of knowledge in terms of lithological and fault distribution (e.g. Hunfeld et al., 2017; Kortekaas and Jaarsma, 2017), as well as the state of stress (e.g. Buijze et al., 2019; Buijze et al., 2017; Van Wees et al., 2017) and the societal impact of induced seismicity on pre-existing faults due to gas
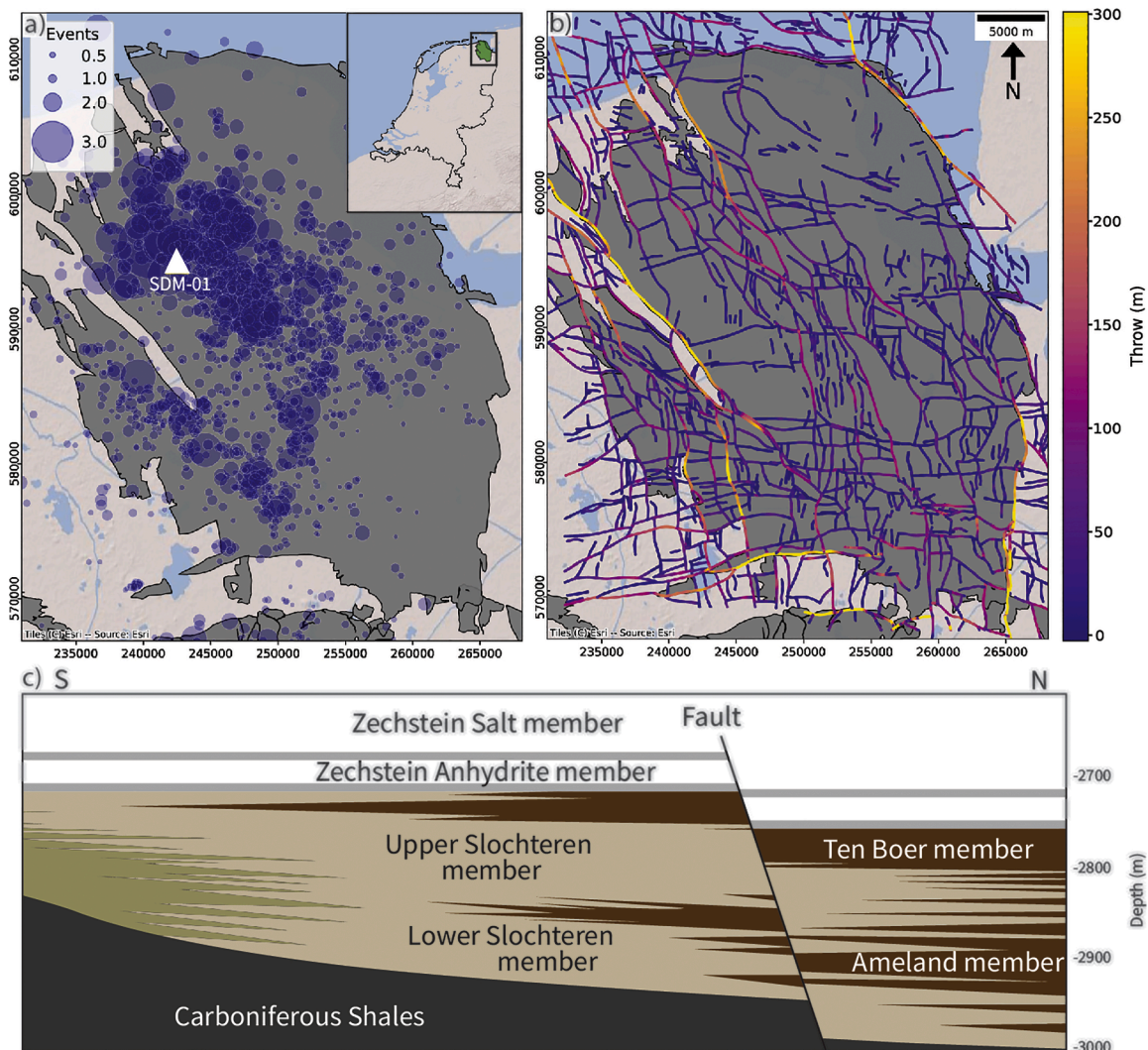
Fig. 1. Geological setting of the Groningen gas field in the northeast of the Netherlands (a) Seismic events recorded by KNMI since 1986 indicated by blue circles (KNMI seismic catalogue retrieved June 2023). Note that most of the seismic epicentres are concentrated in the northwest and southwest of the field. (b) NAM fault model of the Groningen gas field and corresponding fault throw (Bourne and Oates, 2017). (c) Schematic S-N cross-section showing the Groningen stratigraphy (after Van Ojik et al., 2012). From bottom to top: Carboniferous shales, siltstones, sandstones and coal seams, unconformably overlain by the Rotliegend Slochteren and Silverpit formations. A south-to-north proximal-distal trend is characterized by conglomerates in the south, well-sorted aeolian and fluvial sandstone sequences in the central area and clay-rich deposits in the north. The Ameland member of the Silverpit formation divides the Slochteren in a Lower and Upper member. The Ten Boer member is overlain by Zechstein anhydrites, carbonates and a thick sequence of halite. A schematic fault is indicated, highlighting the juxtaposition of mechanically contrasting lithologies. The Stedum-01 (SDM-01) well from which sample were retrieved is indicated by a white triangle.

extraction from the Rotliegend reservoir (e.g. Bourne et al., 2015; Dost et al., 2017; van Thienen-Visser and Breunese, 2015). This reservoir is characterized by a large-scale proximal-to-distal depositional clastic trend, with proximal pebbly and conglomeratic lithofacies in the south, fluvial and aeolian sandstones (the stratigraphic Upper and Lower Slochteren members) in the central area, and more clay-rich lithofacies (the stratigraphic Ten Boer and Ameland members) in the north (Fig. 1c; de Jager and Visser, 2017; Van Ojik et al., 2012). The faults that cut across the reservoir have variable offsets of up to 600 m, juxtaposing mechanically contrasting lithologies in a dense network across the entire region (Fig. 1; Bourne and Oates, 2017).

Previous studies on simulated gouges derived from the Groningen stratigraphy showed that the Slochteren sandstone and Basal Zechstein anhydrite gouges exhibit high friction coefficients whereas Ten Boer and Carboniferous gouges show low friction coefficients (Hunfeld et al., 2017). Only the Basal Zechstein or its homogeneous mixtures with Slochteren sandstone gouges exhibit velocity-weakening behaviour. These results imply that faults in the upper part of the reservoir and its neighbouring overburden would be most sensitive to earthquake nucleation, assuming that only juxtaposing lithologies are present in the fault PSZ (Fig. 1c). Seismological observations available in the Groningen gas field place the hypocentres of most induced earthquake events inside the Slochteren sandstones reservoir (part of the stratigraphic Rotliegend Group), or in the lowermost part of the anhydrites situated at the base of the stratigraphic Zechstein Group, which are located in the immediate overburden of the Slochteren sandstones reservoir (Dost et al., 2020; Smith et al., 2020; Spetzler and Dost, 2017; Willacy et al., 2019). The largest events (Huizinge earthquake of M_L 3.6 and Zeerijp earthquake M_L 3.4) occurred on small-offset normal faults that do not juxtapose the Basal Zechstein against Slochteren (Buijze, 2020). Furthermore, the effects of clay smearing and lithology mixing of the interbedded Ten Boer layer are not well understood. Therefore, a-priori predictions of fault rupture nucleation based only on these lithology compositions are less reliable.

Our aim is to investigate how initial along-fault compositional heterogeneity affects the evolution of the frictional behaviour as a function of a gradually increasing displacement. We simulate the mechanical contrast of a claystone-sandstone lithological mixture in fault gouge experiments by using the natural example of the mixing between the Ten Boer and Slochteren members in the Groningen gas field. Friction experiments were performed in a rotary shear configuration to accommodate large displacements, required to study mixing, clay smearing and strain localization in faults with large offsets. A velocity stepping procedure was conducted to quantify the rate-dependence of friction and its evolution with displacement. Spatial heterogeneity was introduced by segmentation of the simulated gouge in claystone and sandstone patches. Because the frictional properties of low permeability-gouges may be affected by pore fluid pressure transients, monitoring of fluid pressure is required. Four pressure transducers were installed in the vicinity of the simulated gouges and used to monitor the fluid pressure. Microstructural analyses by light microscopy and scanning electron microscopy techniques including backscattered electron imaging (SEM-BSE) and energy dispersive X-ray spectroscopy (SEM-EDX) were performed to identify the mechanisms responsible for the observed frictional evolution and its velocity dependence.

2. Materials and methods

2.1. Sample material

Following the methodology of Hunfeld et al. (2017), we used sample material from the Stedum-01 (SDM-01) well in the seismogenic centre of the Groningen gas field (Table 1). Samples of Ten Boer claystone (TB) and Slochteren sandstone (SL) lithologies were crushed to a fine-grained material to simulate large offset fault gouges. The Ten Boer claystone samples were sieved to a grain size <125 μm. The Slochteren samples

Table 1

Semi-quantitative XRD data for the materials used in this study (data obtained by Hunfeld et al., 2017). The error in XRD data is ±5 %.

| Mineral	Slochteren sandstone (SL)	Ten Boer claystone (TB)
Quartz	67	48
Feldspar	19	7
Phyllosilicates	3	39
Carbonates	6	3
Hematite	-	2
Other	5	-

were not sieved after crushing and have an initial grain size <225 μm (see Supporting Material Fig. S1). The SL gouge contains 67 % quartz, 19 % feldspar, 6 % carbonates and only 3 % phyllosilicates (kaolinite and phengite). The TB gouge contains 48 % quartz, 7 % feldspar, 39 % phyllosilicates (muscovite/phengite and chlorite), and small amounts of carbonates and hematite (Hunfeld et al., 2017).

2.2. Sample assembly and rotary-shear configuration

Each sample contained 35.0 g of simulated gouge and was placed into the sample assembly to form an annular layer (Fig. 2b and c). Spatially homogeneous gouges were equally distributed to form a uniform layer. Spatially heterogeneous gouges were prepared by vertical segmentation of the sample or by horizontal layering, simulating along-fault and fault-parallel variations, respectively. The vertically segmented gouges consisted of equal quadrants of alternating composition (or octants for r313; see Table 2 and Fig. 2c). The horizontally layered sample consisted of two outer SL gouge layers (each 45 wt %) and a TB gouge interlayer (10 wt %). All samples were compressed and levelled manually (±0.1 mm variability in thickness) before emplacement in the rotary-shear apparatus. The sample assembly comprised two grooved piston rings with an inner and outer radius (r_i and r_o) of 35 mm and 50 mm, respectively (Fig. 2b). The imposed velocities and displacements were calculated to the mean radius (r_m) of the sample (42.5 mm). The 0.7 mm deep grooves grip onto the initially ~4.5 mm thick gouge layer. Four pressure transducers (PT) were installed in the lower piston to measure local pore pressures (10 MPa range, 0.008 MPa resolution) in the vicinity of the sheared sample. The sample was radially confined by a tightly fitted inner and outer brass ring and sealed with O-rings (Fig. 2b). Two fluid ports in opposite sides of the outer ring allowed for fluid injection and drainage of the sample. An ISCO-pump was connected to one of the fluid ports to saturate the sample with DI-water. All experiments were performed in a rotary shear apparatus (Fig. 2a) located in the HPT-lab at Utrecht University (see Supporting Material S3 and Korkolis et al., 2021). Acquisition and recording of the mechanical and pore pressure data was done at 1 kHz, using an Elsys TraNET EPC.

2.3. Experimental procedure and data acquisition

After preparing the gouge layer, the sample assembly was placed into the rotary shear apparatus (Fig. 2a). A small normal stress of ~0.4 MPa was applied before saturating the sample with DI-water, using an ISCO pump. The sample was assumed to be saturated after droplets were observed at the opposite fluid port. Once saturation was established, the ISCO-pump was set to a constant pressure of 100 kPa to allow sample drainage through both fluid ports. After the saturation phase, the sample was pre-compacted and allowed to drain for three hours under the desired axial loading conditions (Table 2). Once pore fluid pressures had stabilized, the sample was sheared by applying a rotational velocity. During an initial constant velocity phase, the sample was sheared at 10 μm/s over a mean displacement of 10 mm (or a minimal shear strain of 2.2). This phase comprises yielding, a peak in shear stress and a subsequent approach of a steady-state shear stress (e.g. Haines et al., 2013). After the initial shearing phase, up to five velocity stepping sequences (10–30–100–300–1000–300–100–30–10 μm/s) were imposed to
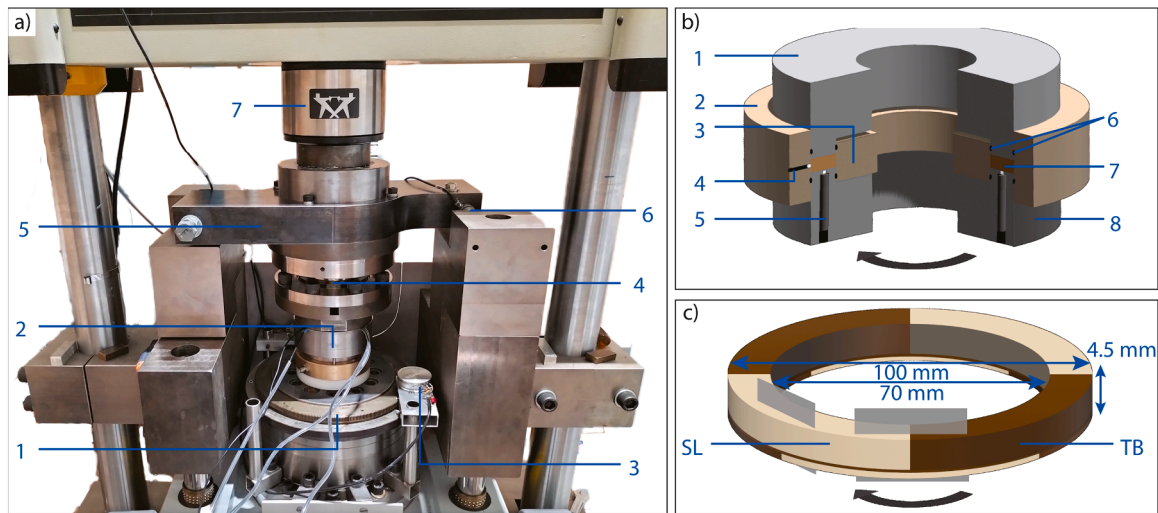
Fig. 2. (a) Rotary shear configuration in the HPT-lab at Utrecht University: 1) rotating driving platter driven by a Parker MH205 motor; 2) sample assembly, shown in (b); 3) one of two angular potentiometers; 4) inline HBM torque sensor; 5) crosshead 6) one of two load cells; 7) Instron load cell. (b) Sample assembly: 1) upper, stationary piston; 2) outer ring; 3) inner ring; 4) pore fluid port; 5) one of four pressure transducers; 6) O-rings for sealing the sample cavity; 7) sample material; 8) lower, rotating piston. (c) Sample distribution for segmented fault gouges comprising two Slochteren sandstone (SL) gouge segments and two Ten Boer claystone (TB) gouge segments. Locations of thin sections as shown in Fig. 6 are indicated.

investigate the velocity dependence of friction and its evolution with displacement (Table 2).

Data on axial load (F_n), axial displacement (H), mean rotational displacement (D_m), torque (T) and local pore fluid pressures ($P_{f,1}$, $P_{f,2}$, $P_{f,3}$ and $P_{f,4}$) were recorded at a rate of 1 kHz (Supporting Material S3). The normal stress (σ_n) was computed by dividing the axial force by the sample surface area (A). The effective normal stress (σ'_n) is defined here as $\sigma'_n = \sigma_n - P_f$. The shear stress ($\tau$) was calculated by dividing the shear force (F_s) at the sample mean radius (r_m) by the sample surface area. The apparent coefficient of friction was computed as $\mu = \tau / (\sigma_n - P_{f,mean})$, assuming that cohesion equals zero. The velocity dependence of μ was determined using a Rate-and-State friction (RSF) approach (Dieterich, 1978, 1979,1981; Ruina, 1983). For comparison with Hunfeld et al. (2017), a Dieterich-type law was used to describe the evolution in frictional strength from a reference steady state value to a new steady state value (Blanpied et al., 1998; Linker and Dieterich, 1992; Marone, 1998). Depending on the frictional response to a velocity step, one or two state variables were used. Values for individual RSF parameters (a, b_1, $D_{c,1}$, b_2, and $D_{c,2}$) as well as the combined rate sensitivity parameter ($a - b$) were obtained for single velocity steps using Xlook Marone et al., n.d. (also see Supporting Material S4).

After every experiment, the sample assembly was taken out of the rotary shear apparatus and the upper piston was removed. The rest of the assembly along with the gouge material was dried in a stove at 50 °C for at least 12 h. After drying, intact sample fragments were collected and impregnated with resin. Thin sections were prepared roughly at the mean radius of the sample, perpendicular to the shear plane and approximately parallel to the shear direction (Fig. 2c). We performed microstructural analyses using light microscopy and SEM (BSE/EDX) by using the Zeiss EVO 15 SEM at Utrecht University.

3. Results

3.1. Mechanical data

3.1.1. Sliding friction

All simulated fault gouges showed an initial rapid near-linear increase in friction until yielding occurred after ~1 mm of displacement (Fig. 3a). The TB gouge subsequently showed strong displacement-weakening, until a steady state residual friction was reached (μ_{ss}=0.27–0.30). After 20 mm displacement, the TB gouge showed minor displacement-weakening (-0.00029 mm^{-1}). Note that displacement-strengthening and -weakening trends are superimposed on transient changes in friction, associated with the velocity steps. The SL gouge exhibited steady state friction coefficients of μ_{ss}= 0.51–0.54. After ~20 mm displacement, near-linear displacement-strengthening (0.00059 mm^{-1}) was observed leading to friction coefficients up to μ_{ss}= 0.6 (Fig. 3a). The homogeneously mixed gouge (TB:SL = 50:50 wt %) showed a peak friction similar to the SL gouge. However, subsequent strong displacement-weakening resulted in lower steady state friction values (μ_{ss}= 0.46–0.49). The sandwiched gouge (SL:TB:SL = 45:10:45 wt %) showed strong displacement-weakening after yielding and a steady state friction above the TB gouge (μ_{ss}= 0.31–0.39). The friction coefficient of the sandwiched sample further deviated from the TB gouge at larger displacements.

Segmented gouges showed a pronounced evolution in their macroscopic friction with displacement (Fig. 3a). The peak in friction was similar to that of the SL gouge. The subsequent phase of strong displacement-weakening (-0.00476 mm^{-1}) led to friction values slightly above the TB gouge and sandwiched gouge ($\mu \approx 0.34$). Strong displacement-weakening was observed up to 35 mm of displacement, followed by the stabilisation of the sliding friction. After ~55 mm displacement (~75° of rotation) pronounced displacement-strengthening was initiated (0.00292 mm^{-1}). Sliding friction stabilized again after 155 mm displacement at values slightly below that of the SL gouge (μ_{ss}=0.52–0.54). Segmented gouges, sheared at different normal stresses (σ_n= 2.5, 5.0, and 10.0) all showed a similar evolution in friction (Supporting Material Fig. S5.2).

Additional experiments were performed to further investigate the microstructural and mechanical evolution of the segmented gouges. Experiment r283 was stopped after ~85° of rotation to obtain microstructural information (see Supporting Material Fig. S7.2). A constant velocity, large displacement experiment (r313) was performed to study how sliding friction evolved after 180° rotation. We observed a periodic change in friction coefficient with a wavelength of ~180° and an amplitude of $\mu \approx 0.05$ (Fig 4a). This periodic change is superimposed on a long-term displacement-strengthening trend (0.00047 mm^{-1}). Maxima in sliding friction are similar to the steady-state friction of SL gouge and minima are similar to that of the mixed gouge (Fig. 4a). Changing the sample from a quadrant to an octant distribution (i.e., eight equal segments of alternating SL and TB gouge) leads to a factor two period

Table 2

List of experiments and conditions. All experiments were performed at room temperature and under drained conditions. Mean displacements (D_m) were determined at the mean radius of the sample (r_m = 42.5 mm) and correspond to the lower piston rotation (θ). Velocity sequences are denoted by VST = velocity stepping test, followed by the number of sequences and CVT = constant velocity test followed by the velocity (μm/s). Velocity stepping sequence consists of steps 10–30–100–300–1000–300–100–30–10 μm/s. Weight percentages of TB gouge and SL gouge are given. Seg. denotes the number of vertical segments.

Exp.	Wt % TB/wt % SL	Seg.	σ_n (MPa)	Pore Fluid	D_m (mm)	θ (°)	V-sequence
Homogeneous gouge mixtures							
r218	0/100	1	5.0	Dry	~145	~195	VST–5
r269	0/100	1	5.0	DI-water	~145	~195	VST–5
r291	0/100	1	5.0	DI-water	~145	~195	VST–5
r281	30/70	1	5.0	DI-water	~145	~195	VST–5
r220	50/50	1	5.0	DI-water	~145	~195	VST–5
r282	70/30	1	5.0	DI-water	~145	~195	VST–5
r217	100/0	1	5.0	Dry	~145	~195	VST–5
r212	100/0	1	5.0	DI-water	~145	~195	VST–5
r219	100/0	1	5.0	DI-water	~145	~195	VST–5
Spatially heterogeneous gouges (sandwiched)							
r222	10/90	1	5.0	DI-water	~145	~195	VST–5
Spatially heterogeneous gouges (vertically segmented)							
r287	50/50	4	5.0	DI-water	~145	~195	No shearing
r277	50/50	4	5.0	DI-water	~145	~195	VST–5
r289	50/50	4	2.5	DI-water	~145	~195	VST–5
r290	50/50	4	5.0	DI-water	~145	~195	VST–5
r286	50/50	4	10.0	DI-water	~145	~195	VST–5
r283	50/50	4	5.0	DI-water	~65	~90	VST–2
r313	50/50	4	5.0	DI-water	~300	~405	VST-1 + CVT-100
r312	50/50	8	5.0	DI-water	~550	~740	VST-5 + CVT-100

decrease (See experiment r312; Supporting Material Fig. S5.3).

3.1.2. Volumetric behaviour and pore pressure evolution

All homogeneous gouges showed an initial phase of strong shear induced compaction, followed by slowly decaying compaction towards a constant layer thickness (Fig. 3b). The shear-induced compaction of the TB gouge is significantly smaller than that of the SL gouge, mixture and sandwiched gouge. No dilatancy was observed in any of the homogeneous gouges. In contrast, segmented gouges showed periodic dilatancy and compaction, corresponding to the periodic displacement-strengthening and displacement-weakening, respectively (Figs. 3b and 4b). The high stiffness of the pistons does not allow for strong differential compaction in segmented gouges. Tests with pressure-film show that after the pre-compaction phase, stresses are more concentrated on the SL segments (Supporting Material S9).

The evolution of the pore fluid pressure versus displacement (Fig. 3c) shows that the initial shear-induced fluid pressurization was considerably larger in the segmented gouge when compared with other gouges (>0.75 MPa vs 0.02 - 0.35 MPa; Fig. 3c). The segmented gouges were also more susceptible to pressure transients following high velocity steps. During the first two velocity-stepping sequences, high-velocity steps caused pressurisation of the sample, whereas subsequent

shearing only caused drainage. Homogeneous gouges showed only drainage after the initial pressurisation phase. Large differences in local pore pressures were only observed in segmented gouges (Supporting Material Fig. S5.4).

### 3.1.3. Velocity dependence of friction

Individual rate-and-state friction (RSF) parameters as well as the rate sensitivity parameter (a-b) were determined for velocity upsteps from 10 to 30 μm/s (Fig. 3d and Fig. 5). Only the SL gouge required a RSF law with two state-variables to fit the data (Supporting Material S4). Positive values (a-b>0) indicate velocity-strengthening behaviour and negative values (a-b<0) indicate velocity-weakening behaviour. The TB gouge and sandwiched gouge only showed velocity-strengthening behaviour and no significant displacement dependence (Fig. 3d). In contrast, the SL gouge showed only velocity-weakening and an increase in (a-b) with displacement. The mixed gouge also showed a displacement dependence of (a-b) but with an opposite trend (Fig. 3d). All gouges showed similar values for the direct effect a (Fig. 5a). Differences arise in the evolutionary effect b_1 (and b_2 for the SL gouge). The lowest b_1 values were observed in the TB and layered gouges, whereas the SL gouges showed the highest values. A second evolutionary effect with negative b_2 values was obtained for the latter, showing a decrease with displacement (Fig. 5e). This decrease in b_2 coincided with an increase in critical slip distance D_{c2} (Fig. 5f). All gouges showed an increase in (a-b) with increased load-point velocity (V_{lp}) for all displacements with the exception of the SL gouge (Supporting Material Fig. S6.2). This gouge showed an opposite relation at large displacements.

Segmented gouges showed a pronounced increase in (a-b)-values with displacement at all load-point velocities (Fig. 3d). At low load-point velocities this increase caused a transition from velocity-weakening to velocity-strengthening behaviour. The a values of the segmented gouges are similar to all other gouges and showed no displacement dependence (Fig. 5a). The b_1 values of the segmented gouge decreased with displacement and showed the largest change compared to the other gouges. At small displacements, (a-b)-values of the segmented gouge closely resembled the behaviour of the SL gouge and at large displacements, that of the TB gouge (Fig. 5c). Interestingly, the increase in friction after ~90° of rotation was not accompanied by a decrease in (a-b)-values (Fig. 3a and d).

3.2. Microstructures

SEM-BSE images of the homogeneous gouges (Fig. 6) are used to distinguish between the relatively undeformed bulk gouge and the principal slip zone (PSZ) that accommodates most of the shear. The latter is defined by a zone of reduced grain size and porosity and the presence of shear foliations associated with the main shear zone (R_1, R_2, P and Y-shears; Logan et al., 1979), although their separation is not always fully clear.

The bulk TB gouge is characterised by sub-angular quartz grains and phyllosilicate aggregates up to ~125 μm in grain size, embedded in a fine grained (< 20 μm) phyllosilicate matrix. Intergranular microfractures, present in the bulk gouge (possibly related to unloading before sample retrieval) are predominantly oriented in the R_1- and Y-shear direction (Fig. 6a). A well-defined 30–100 μm wide PSZ, characterised by a substantially smaller grain size and the absence of phyllosilicate aggregates, is observed at the lower bound of the sample (Fig. 6a-b). The SL gouge predominantly contains quartz grains (<225 μm) embedded in a fine-grained matrix of phyllosilicates, feldspar and quartz. The sheared SL gouge has a 1000 – 1400 μm wide zone of reduced porosity compared with the bulk sample (Fig. 6c). The lower boundary of this zone is located at the top of the grooves in the lower piston and is characterised by grain size reduction (< 20 μm; Fig. 6d). This narrow boundary is interpreted as the PSZ. The 50:50 wt % gouges mixture has a 700 – 1000 μm wide zone of reduced porosity in the vicinity of the lower piston (Fig. 6e). Phyllosilicate aggregates up to 125
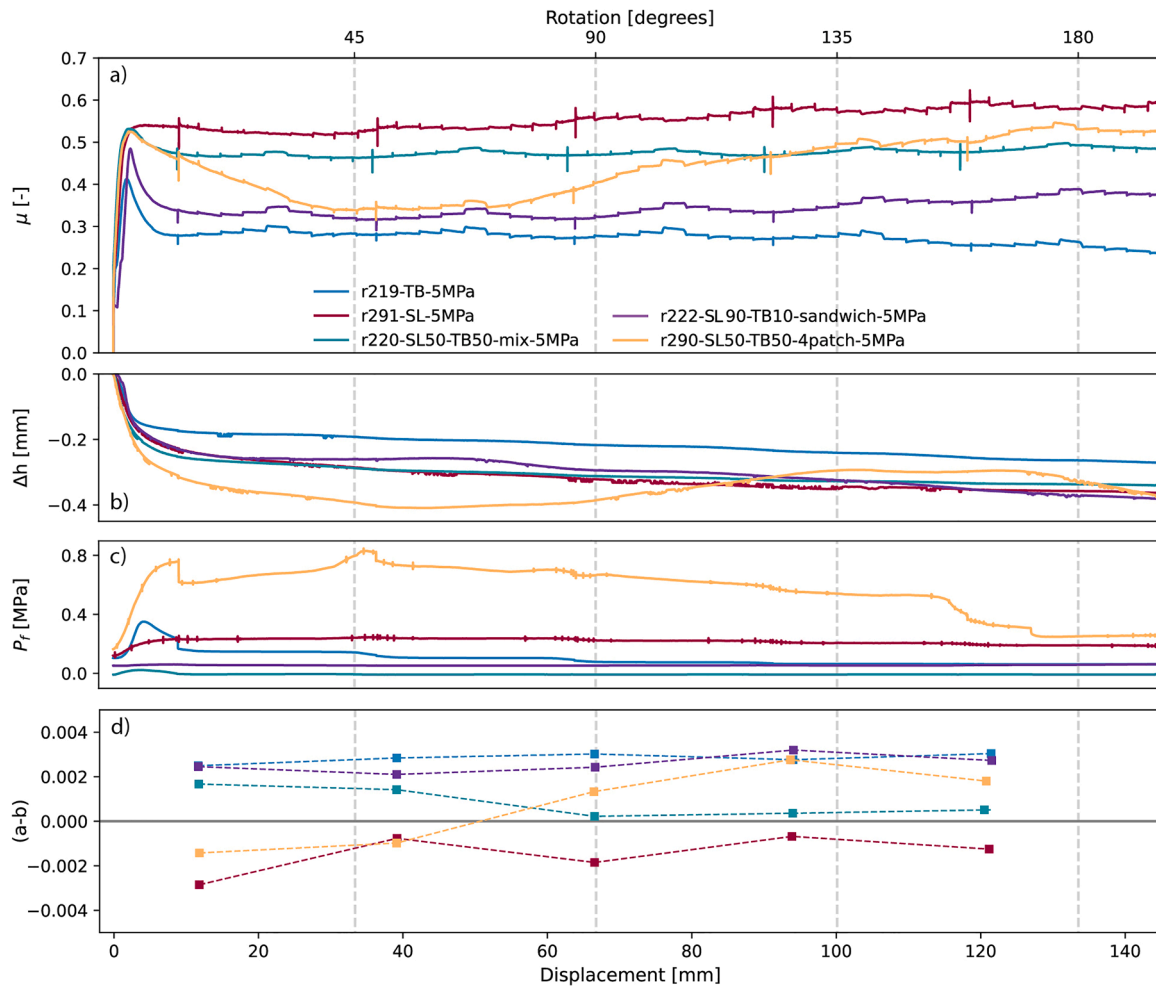
Fig. 3. Mechanical data obtained in this study. (a) Sliding friction (μ) versus displacement. Friction coefficients are corrected for average pore fluid pressures. Note that displacement-weakening/strenghtening trends are superimposed on the frictional response to velocity steps. Five velocity stepping sequences (10–30–100–300–1000–300–100–30–10 μm/s) were imposed to obtain the rate-dependence of friction as shown in Fig. 5. (b) Shear-induced sample thickness change versus displacement. (c) Pore fluid pressure versus displacement computed as average of the local pore pressures. (d) Combined RSF-parameter (a-b) versus displacement for velocity steps of 10–30 μm/s. The segmented gouge shows a pronounced increase in (a-b) from a velocity-weakening regime to a velocity-strengthening regime. After the development of a continuous clay-smear (>90° rotation), (a-b)-values become larger than those of the mixed gouge (r220; homogeneous equivalent of segmented gouges in terms of composition).

μm in size are present in the bulk gouge (upper part of the sample and within the grooves of the lower piston) but are lacking in the zone of reduced porosity (Fig. 6f). The lower boundary of this zone is defined by a sharp Y-shear, cutting off phyllosilicate aggregates. The upper boundary is defined by opening fractures.

The segmented gouge shows the presence of a PSZ near the lower piston (Fig. 7a). The PSZ predominantly contains phyllosilicates derived from the TB gouge, smeared between the lower piston and the two different bulk gouges and is referred to as a clay smear. The bulk gouges are located above the PSZ and between the grooves of the rotating lower piston and have particle size distributions similar to those of the starting materials. The boundaries between the PSZ and the bulk TB gouge are relatively sharp, flat and undisturbed interfaces (Fig. 7a and e). The boundary between the PSZ and the bulk SL gouge is less well-defined and is characterized by zones of mixing (Fig. 7f and 8a; see also Supporting Material Figs. S8.1 and S8.2). Large quartz grains in this zone dominate the local orientation of the foliation (Figs. 7c and 8a). The PSZ itself shows large variations in width, ranging between 150 and 500 μm when smeared between SL gouges, and between 10 and 200 μm when in contact with TB gouge (Fig. 7a). Towards the TB-SL interface, the PSZ widens up to ~600 μm and the upper boundary connects with a R_1-shear in the SL gouge. Phyllosilicates within the PSZ show a wavy foliation in

the P-shear and Y-shear direction or around large quartz grains (Fig. 7b, c and Fig. 8a). Long (> 5 mm) continuous Y-shears only develop in the absence of such large grains (Fig. 6b). Sections further away from the initial TB-SL interface show a larger abundance of quartz grains within the PSZ and hence, no continuous Y-shears (Figs. 7f and 8a). At larger displacements, the clay smear becomes wider and shows alternating layers with variations in the amount of quartz grains (see Supporting Material Fig. S7.2f vs i).

The sandwiched gouge contains a phyllosilicate interlayer with a similar width as the PSZ in the segmented gouge (~400 μm). However, mixing zones are lacking and shear is localized within the phyllosilicate layer (Fig. 8b). In contrast to the segmented gouge, the boundaries of the PSZ are characterized by sharp and flat continuous Y-shears. The TB gouge outside the PSZ still contains intact or partly fractured phyllosilicate aggregates. Opening fractures in P_1 and P_2 orientation are abundant in the sandwiched gouge.

4. Discussion

4.1. Effects of gouge composition on sliding friction and rate dependence

Our results show that the quartzofeldspathic-rich SL gouges exhibit
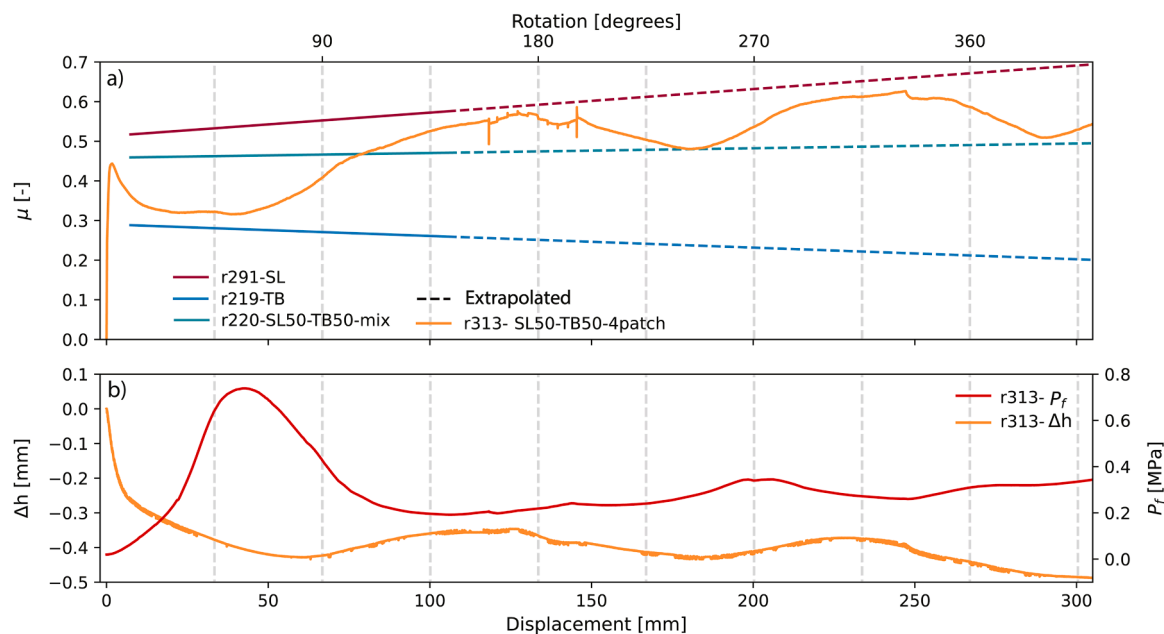
Fig. 4. Mechanical data of segmented large displacement experiment r313. A constant mean velocity of 100 μm/s was applied, with the exception of one velocity stepping sequence at ~180° of rotation. (a) Sliding Friction (μ) versus displacement. The red, green and blue lines are computed trendlines with extrapolated (dashed) displacement-weakening/strengthening trends for the SL gouge, mixed gouge and TB gouge respectively (see Fig. 3a). (b) Shear-induced sample thickness change (Δh) and mean pore fluid pressure (P$_f$).

significantly higher steady state sliding frictions than the clay-rich TB gouges (μ_{ss}= 0.51–0.54 vs μ_{ss}=0.27–0.30). This is consistent with the research of Hunfeld et al. (2017) and other previous studies that showed reduced fault strength in phyllosilicate-rich gouges, especially in the presence of fluids (Byerlee, 1978; Crawford et al., 2008; Giorgetti et al., 2015; Moore, 2004; Tembe et al., 2010). Our results also show that the gouge composition has an important effect on the velocity dependence of friction. We observed a velocity-strengthening behaviour of the weak phyllosilicate-rich TB and mixed gouges, in contrast to the velocity-weakening behaviour of the strong SL gouges. This is consistent with previous experiments that showed an inverse relationship between fault strength and the combined RSF parameter (a-b) (Bedford et al., 2022; Ikari et al., 2011). Hunfeld et al. (2017) also reported velocity-strengthening behaviour for the TB gouges. In contrast to our results, they also observed velocity-strengthening in the SL gouges. We suggest that this discrepancy can be explained by the very small shear strains obtained in Hunfeld et al. (2017) compared to our ring-shear experiments. This inference is in agreement with previous studies that demonstrated the requirement of a critical amount of accumulated shear strain for quartzofeldspathic gouges to become velocity-weakening through shear localization (Beeler et al., 1996; Ikari et al., 2011; Leeman et al., 2016; Noël et al., 2023; Scuderi et al., 2017). Microstructures of our SL gouges show the presence of a PSZ defined by local grain size reduction (Fig. 6c-d), suggesting that shear-localisation has occurred.

The values of the direct RSF parameter a are similar for all gouges tested in our study (Fig. 5a). The differences in (a-b) between the SL gouge and TB gouge are thus attributed to a difference in the evolutionary response parameter b. The value of b might be interpreted as a measure of the frictional strength change following the evolution of the real contact area (Dieterich, 1979, 1981; Ikari et al., 2009). In this context, positive b values reflect a decrease in real area of contact with increasing velocity, presumably due to dilatancy. The small b values in our phyllosilicate-rich TB gouge suggest a lack of changes in real area of contact, possibly due to the characteristic platy structure of the grains and the tendency of these grains to readily compact and align (Ikari et al., 2009). The SL gouges show a large drop in friction (b$_1$), suggesting dilatancy upon velocity increase. This decrease in friction is followed by

a second, opposite or negative evolution effect (b$_2$). A negative evolutionary effect cannot easily be explained by a changing contact area. Previous explanations for negative b-values include kinking of phyllosilicate grains (Ikari et al., 2009), transient changes of the thickness of the fluid film between grains (Niemeijer and Collettini, 2013), or the mechanical effect of a pore fluid pressure drop as a result of dilatation and undrained conditions (Ikari et al., 2009). These proposed mechanisms might be valid for phyllosilicate-rich gouges, but less appropriate for our quartzofeldspathic-rich SL gouge at relatively low effective normal stress, because sufficient permeability under these conditions allows rapid fluid overpressure drainage (i.e. short fluid diffusion times; also see Ikari et al., 2009). We speculate that the observed increase in D$_{c2}$ (Fig. 5f) might be related to localisation and progressive comminution in the principal slip zone.

4.2. Frictional evolution of segmented gouges

Segmented gouges exhibited both an evolution in sliding friction and velocity dependence. We observed a phase of strong displacement-weakening after yielding, followed by a phase of strong displacement-strengthening (Fig. 3a). Our large-displacement experiments showed a subsequent phase of periodically changing sliding frictions with maxima similar to the steady state friction of the SL gouge and minima similar to that of the 50:50 wt % mixed gouge superimposed on a long-term displacement-strengthening trend (Fig. 4a). The evolution in velocity dependence is characterised by progressively larger (a-b). We discuss further possible mechanisms responsible for the observed trends in frictional behaviour.

4.2.1. Strain partitioning and microstructural evolution

The initial strong displacement-weakening observed in segmented gouges can be partly attributed to clay smearing over a progressively larger sample area, in combination with shear localisation on foliation planes within the clay smear as previously proposed by Bedford et al. (2022). Other experimental studies have shown that only a small amount of a weak phase could be enough to weaken a gouge significantly, once an interconnected and throughgoing zone of foliated gouge
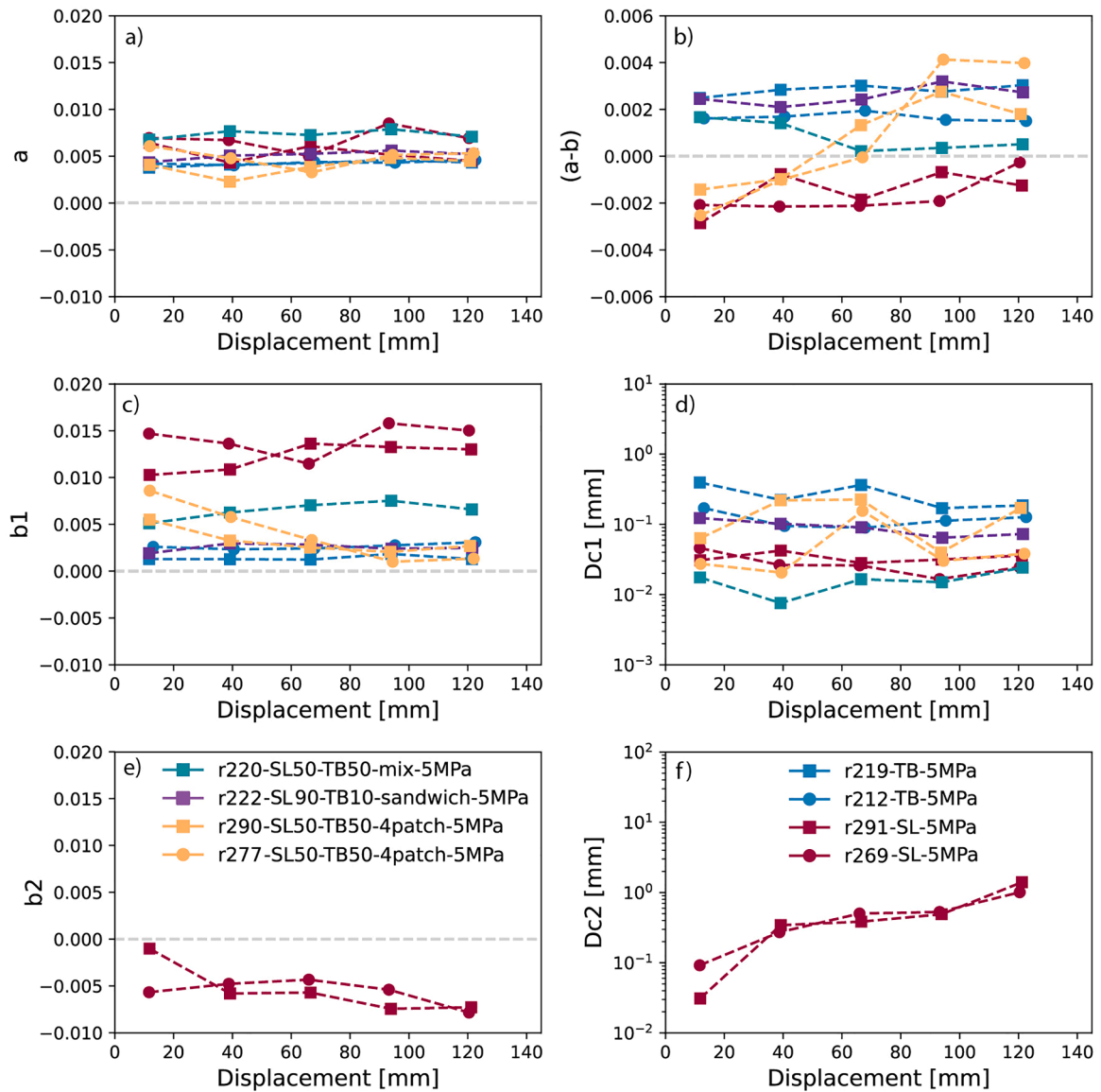
Fig. 5. Rate-and-state friction data for velocity up-steps of 10–30 µm/s. The combined rate-sensitivity parameter (*a-b*) and the individual parameters *a*, *b₁*, and D_{c1} are plotted against displacement. For the SL gouges (r291 and r269), a second state variable *b₂* and corresponding critical slipping distance D_{c2} were required to fit the data. Note that differences in (*a-b*) values between different gouges are attributed to the evolutionary effect(s) *b₁* and *b₂*. The segmented gouges showed the largest evolution in b₁ and (*a-b*) with displacement.

of a minimum critical thickness has formed, which depends on the grain size of the strong phase (Collettini et al., 2009, 2019; Giorgetti et al., 2015; Moore and Lockner, 2011; A. Niemeijer et al., 2010; Rutter et al., 2013). The observed displacement-weakening coincides with an increase in (*a-b*). Within the first 90° of rotation, this increase leads to a transition from velocity-weakening to velocity-strengthening (Fig. 5c). The changing velocity dependence is attributed to a change in the evolutionary response parameter *b* (Fig. 5a-c). The observed decrease in *b* suggests that with shear-displacement, porosity and the real area of contact evolve less upon a step in velocity. This inference is in agreement with the idea that progressively more shear is accommodated by foliation planes within the phyllosilicate-rich clay smear. The microstructures of our segmented gouges confirm the development of a thin (150 – 500 µm wide) clay smear over the full sample area after 90° of rotation (Supporting Material Figs. S7.1 and S7.2a-c).

After the initial phase of weakening, we observed strong displacement-strengthening followed by periodic variations in friction coefficient and sample thickness (Fig. 3a-b and Fig. 4). Microstructural observations show that the clay smear width and abundance of

quartzofeldspathic grains within the smear increase with displacement (Supporting Material Fig. S7.2). We interpret that the clay smear development involves sand-clay mixing as an integral part of the smearing mechanism (Vrolijk et al., 2016) and references therein). This is confirmed by the notable differences in PSZ boundaries between the segmented gouges and the sandwiched gouge (Fig. 7). A possible mechanism for the observed displacement-strengthening is the progressive widening and incorporation of quartzofeldspathic grains into the PSZ. The latter process does not lead to a decrease in (*a-b*)-values (Fig. 5c). In fact, *b* values only decrease with displacement, suggesting that shear remains predominantly accommodated on phyllosilicate foliation planes. However, the abundance of quartzofeldspathic grains prevents throughgoing continuous Y-shears to be sustained (Figs. 7f and 8a). Therefore, strain must be partly accommodated by steeper foliation planes, resulting in a larger sliding friction.
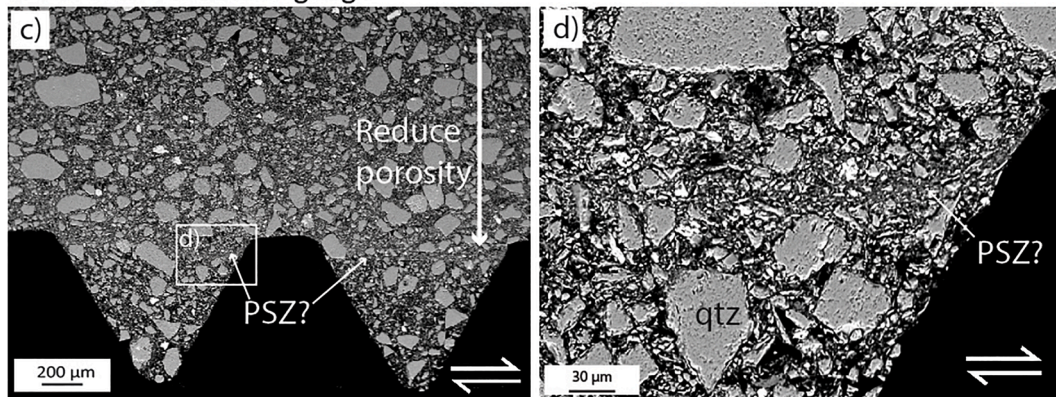
The observed periodicity in friction coefficient and volumetric behaviour is roughly proportional to sample segment size and the amount of rotation (Supporting Material Fig. S5.3). This is possibly caused by: (1) The effect of pore fluid pressure transients, coupled to the
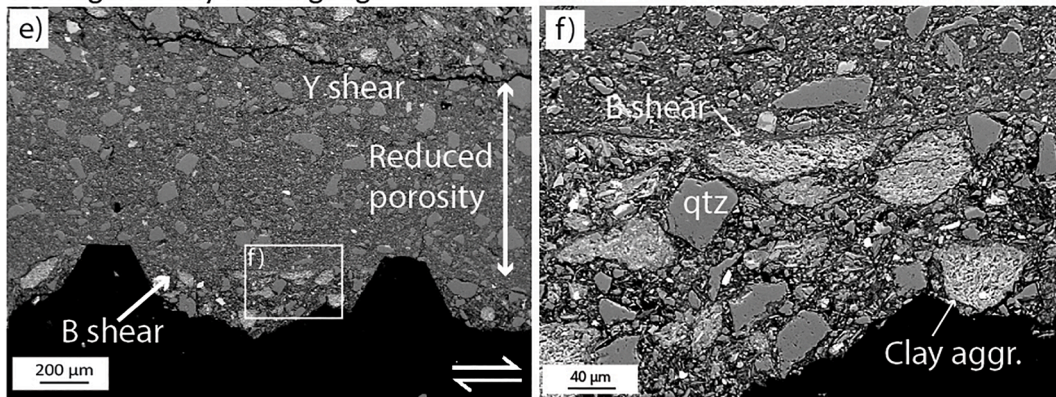
Ten Boer claystone gouge
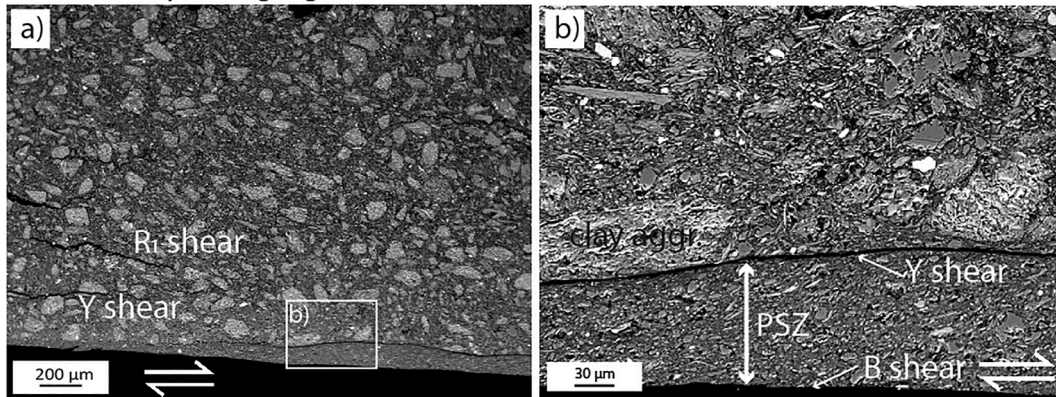
Slochteren sandstone gouge


Homogeneously mixed gouge

Fig. 6. SEM-BSE images of the homogeneous gouges after ~145 mm of mean displacement. (a-b) Typical Ten Boer claystone microstructures (r219) showing a narrow principal slip zone (PSZ) at the bottom of the sample. R_1-shears and Y-shears are present throughout the bulk sample. Phyllosilicate aggregates are only preserved within the bulk gouge. (c-d) Slochteren sandstone gouge (r291) exhibiting a zone of reduced porosity towards the bottom piston. A 10–30 μm wide zone of reduced grain size is present only directly above the piston grooves and is interpreted as PSZ. (e-f) Homogeneously mixed gouge of TB:SL= 50:50 wt % (r220) typically showing a zone of reduced porosity above the lower piston. This zone is bound by Y-shears and B-shears and lacks the presence of large clay aggregates. Clay aggregates are, however, preserved in the upper part of the sample as well as between the grooves of the lower piston.

gouge distributions and locations of drainage locations (fluid ports); (2) The interplay between the PSZ and the juxtaposition of bulk gouges, coupled to the upper and lower piston. Periods of displacement-strengthening and dilatation correspond to increased SL-SL juxtaposition and periods of displacement-weakening and compaction correspond to increased SL-TB juxtaposition. Note that juxtaposition in this context does not mean that bulk gouges coupled to the upper and lower piston are in direct contact. After 90° of rotation, juxtaposing bulk gouges are always separated by a thin clay smear or PSZ, having an upper and lower interface with the bulk gouges coupled to the upper and lower piston, respectively (Fig. 7; also see Supporting Material S7).

Microstructural observations show that the characteristics of the interface between the clay smear and the bulk gouge is highly dependent on the type of bulk gouge. The interface between the clay smear and the SL gouge is characterised by large amplitude variations and inclined foliation planes (Fig. 7d, f and Supporting Material Fig. 8.2). In contrast, the interface between the PSZ and the bulk TB gouge is rather sharp and characterised by continuous low-angle foliation planes (Fig. 7e and Supporting Material Fig. 8.2). As the lower piston is rotating, the PSZ will be confined by continuously changing interfaces corresponding to the juxtaposition (Supporting Material Fig. S7.2). Previous experiments systematically tested the effects of gouge thickness (*d*) and piston groove
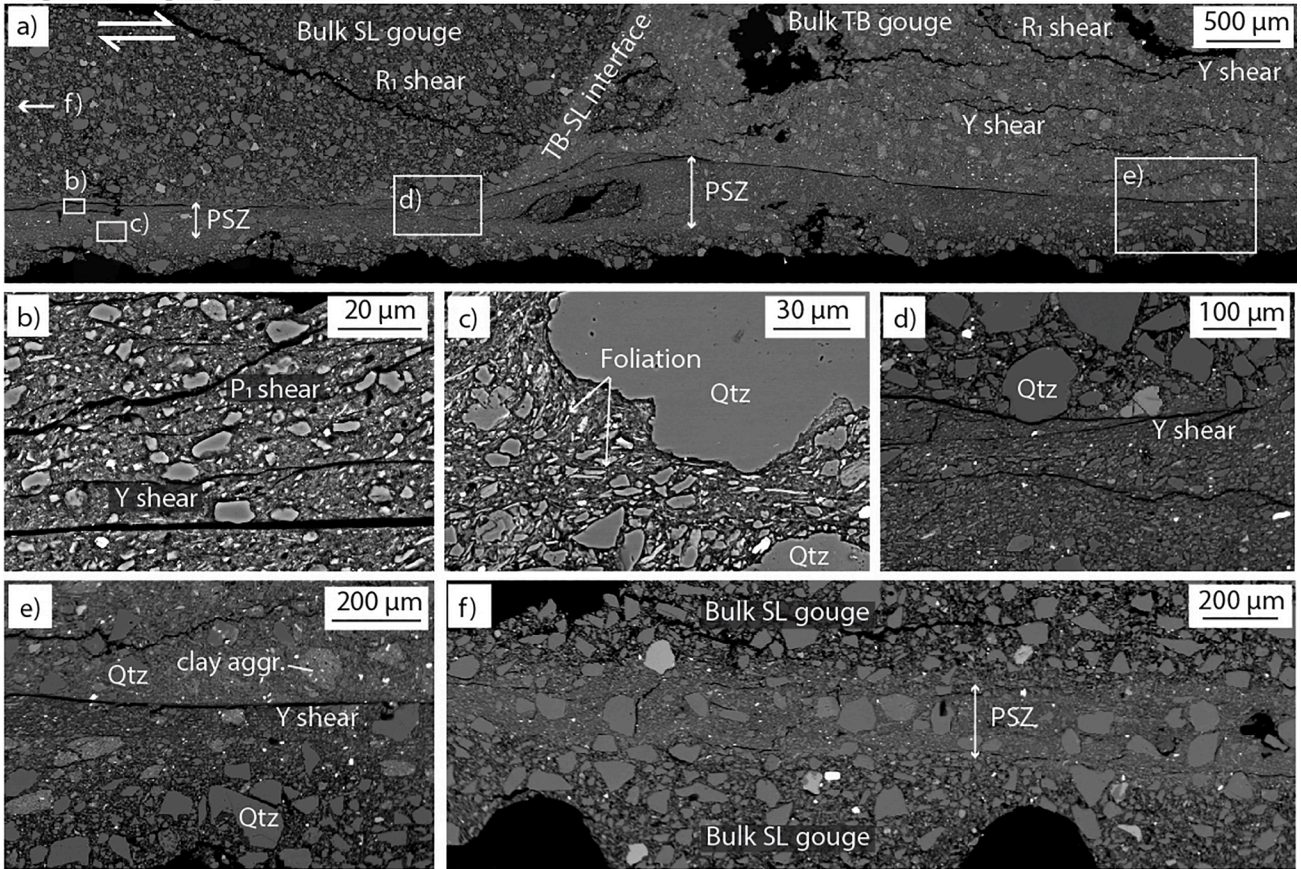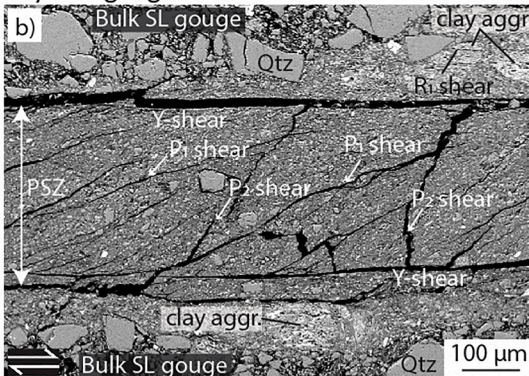
Fig. 7. SEM-BSE images of segmented gouge r290 after ~145 mm of mean displacement. (a) Section at interface between SL gouge (left) and TB gouge (right; also see Fig 2c for location). The interface is tilted at an angle of ~30° from vertical and a boundary shear is visible above the lower piston. Y-shears are present in the TB gouge and R_1-shears are observed in both bulk gouges. The phyllosilicate-rich boundary shear is confined by SL gouges in the left part of the micrograph whereas a contact with less deformed TB gouge containing clay aggregates marks the upper boundary in the right part of the section. (b) Upper section of the clay smear showing the presence of P-shears and throughgoing Y-shears. Note the absence of large quartzofeldspathic grains in this section. (c) Large quartz grain within the clay smear. The foliation bends around the large quartz grain. (d) Interface between bulk SL gouge and clay smear. (e) Narrow Y-shear between bulk SL gouge (bottom) and bulk TB gouge (top). (f) Section within the SL domain (see Fig. 2c) showing the abundance of quartz grains within the clay smear. Note that continuous Y-shears are absent in this section.
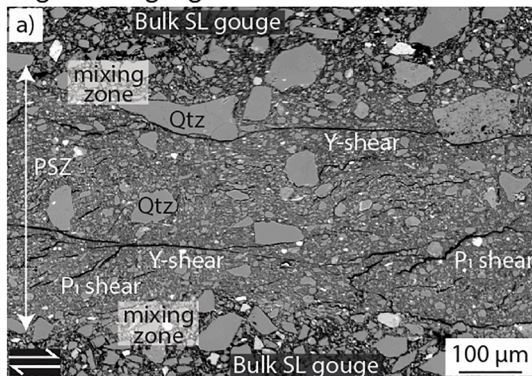
Fig. 8. SEM-BSE images for comparison between segmented gouge (r290) and sandwiched gouge (r222) after ~145 mm of mean displacement. (a) Segmented gouge showing clay smear between bulk SL gouges. The boundaries of the clay smear are characterised by zones of mixing where porosity is reduced, and large quartz grains are embedded in a matrix of predominantly phyllosilicates. Y-shears and P_1-shears are present within the clay smear but are often disturbed by large quartz grains or are not continuous. No clay aggregates are present within the clay smear. We interpret that the principal slip zone (PSZ) includes the zones of mixing (zones of reduced porosity). (b) Sandwiched gouge, showing a zone of strongly foliated, phyllosilicate-rich gouge, bounded by sharp, continuous Y-shears. The phyllosilicate-rich gouge outside the Y-shears is less foliated and still contains intact or partly fractured clay aggregates. Note that the width of the phyllosilicate-rich layer is similar in both gouges but that the PSZ in the sandwiched gouge is smaller.

height (*h*), on the frictional resistance to shearing (Indraratna et al., 2005). Below a critical ratio of gouge thickness and piston groove hight (*d/h*), an increase in frictional resistance and sample dilatation is observed. Both observations were attributed to an interference between the gouge and the pistons, resulting in shear localisation on the inclined shear planes.

As we observed, during SL-SL juxtaposition, the width of the clay smear is rather small compared to the large amplitude variations of the interfaces on both sides, representing a small *d/h* ratio, analogous to the experiments of Indraratna et al. (2005). The resulting interference between PSZ and bulk gouge explains the periodic peaks in friction and dilatancy. During SL-TB juxtaposition, the interfaces with the PSZ are sharp and continuous, leading to a smaller *d/h* ratio, less interference, and hence the observed minima in friction and sample thickness. Interference of the PSZ with the bulk gouge can lead to incorporation of quartzofeldspathic grains into the clay smear. As this is an irreversible process, the quartzofeldspathic content of the PSZ only shows a progressive increase with displacement. A small mismatch between the rotation and periodicity in sliding friction (i.e. peaks at 85 instead of 90°) might be caused by slight irregularities upon assembly of the top piston, and subsequent differential compaction of the segments.

4.2.2. Stress concentration and redistribution

We observed stress concentrations on the SL gouge segments after pre-shear compaction, which is consistent with modelled stress distributions for segmented faults (Buijze, 2020). We expect that normal stresses become more equally distributed with displacement due to increased grain reorganisation and comminution in the highly stressed SL segments as indicated by the development of elevated pore pressures and due to a rotation of the principal stress axes with the onset of shearing (Knuth et al., 2013). Accordingly, normal stresses on the TB gouge segments will increase and sliding friction will become less dominated by the SL gouge segments. The stress redistribution possibly attributes to the initial displacement-weakening as previously suggested by Bedford et al. (2022). Stress redistribution (through grain reorganisation and comminution) and clay smear development are simultaneously operating mechanisms. Once a continuous clay smear has developed over the full sample area, the stresses are assumed to be more or less equally distributed. We only report the macroscopic average bulk friction coefficient as it is impossible to measure local variability in stresses in our experimental setup.

4.2.3. Pore fluid pressure transients

Previous studies have shown that pore pressure transients can affect fault friction and stability, especially in low permeability fault-gouges (Faulkner et al., 2018). In our experiments, segmented gouges show the largest compaction and produce larger pore fluid pressures during the onset of shearing when compared with homogeneous gouges (Fig. 3b-c). We suspect that the high pore fluid pressures are caused by a combination of high-pressure generation rates in the SL gouge and low drainage rates in the TB gouge. The fluid ports are initially located in the TB segments and approximately at the sample height where the clay smear develops (Supporting Material Fig. S7.1). This initial configuration may inhibit full sample drainage. Our presented friction coefficients are corrected for the measured mean pore fluid pressure. However, pressure transducers were located in the rotating bottom piston, at a small distance to the PSZ, causing possible delays and damping effects. If pore pressures in the PSZ are higher than the observed pore pressures at the bottom piston, part of the initial displacement-weakening can be attributed to an initial increase in pore fluid pressure.

Observed trends in the large displacement experiments suggest a link between volumetric behaviour and the evolution of pore fluid pressure (Fig. 4b). However, to explain the amplitude of friction oscillations (~0.05) after 90° of rotation, pore pressure oscillations in the order of 0.5 MPa are required, which are not observed (Fig. 4b).

4.3. Implications for faults in the Groningen gas reservoir

We showed that Slochteren sandstone derived fault gouges exhibit velocity-weakening behaviour after a critical amount of displacement which suggests that a large extent of the reservoir might be prone to earthquake nucleation. This is consistent with the seismological hypocentre estimations predominantly within the Rotliegend reservoir (Spetzler and Dost, 2017; Willacy et al., 2019). The velocity-weakening behaviour of the Slochteren gouge could also explain why the large Huizinga and Zeerijp events occurred on small offset normal faults that do not juxtapose the Basal Zechstein against Slochteren.

Our results further show that juxtaposition of reservoir sandstones against phyllosilicate-rich layers does lead to an increase in frictional stability. This implies that faults in the Groningen field with larger offset have a smaller fault area that is prone to earthquake nucleation compared to faults with smaller offset in a similar stratigraphy. Faults in the north of the Groningen field are expected to be less prone to earthquake nucleation as more phyllosilicate-rich intervals are present (Fig. 1c). Juxtaposition of the reservoir sandstones against phyllosilicate-rich intervals (Ten Boer and Ameland members and Carboniferous formation), is not expected to reduce macroscopic strength of large fault sections as mixing is an integral part of clay smear development along the layered stratigraphy.

Our results have important implications for modelling fault rupture nucleation, propagation and arrest and hence assessing hazards and risks associated with stress changes in the subsurface. They show that frictional properties of juxtaposing faults are not simply represented by the weakest phase (Ten Boer claystone) or by a homogeneous mixture of the weak phase and strong phases (e.g., Slochteren sandstone). However, we note that healing processes on a geological time scale are not accounted for in our experiments and might have an important influence on the cohesion and fault strength of the faults in the Groningen gas field.

5. Conclusions

Along-fault heterogeneity is observed in all fault zones that cross-cut lithological layering. The sliding friction and mechanical stability of such shear zones is controlled by the reactivation and slip behaviour of the fault gouge. Therefore, understanding how fault gouges in a multilayered stratigraphy develop is crucial for predicting fault frictional behaviour.

We performed friction experiments in a rotary-shear configuration to study the effects of along-fault heterogeneity on its frictional behaviour. We find that segmented gouges exhibit an evolution in sliding friction and their rate-dependence. Clay smearing and shear localisation within the clay smear initially cause strong displacement-weakening. However, lithology mixing as an integral part of the clay smearing process is interpreted to counteract the weakening effects when overlap of the stronger layers occurs at larger displacements. Lithology mixing prohibits that a fault segment remains weak with progressive shear. Periodicity in sliding friction and sample dilatation/compaction are caused by the alternations in juxtaposition. When only a thin clay smear separates two sandstone intervals, interaction of the clay smear with the bulk gouges is interpreted to cause an increase in friction. Clay smearing affects the rate-dependence of friction as it shifts it towards velocity-strengthening behaviour with progressive shearing.

Our large-displacement experiments also show that Slochteren sandstone gouge exhibits velocity-weakening behaviour related to strain-localisation in a principal slip zone with reduced grain size. It suggests that faults within the Slochteren sandstone reservoir are prone to earthquake nucleation which explains better the depth intervals of the observed hypocenters when compared to previous experimental studies.

We show that fault friction and the rate-dependence of friction are not simply governed by the weakest lithology along a fault plane and the frictional properties cannot be represented by a homogeneous mixture

of the juxtaposing lithologies. Knowledge on stratigraphic layering in combination with fault throw is required to predict the macroscopic frictional behaviour of fault sections.

CRediT authorship contribution statement

Job P.B. Arts: Conceptualization, Experimental work and Microstructural analysis, Data curation, Formal analysis, Investigation, Methodology, Resources, Validation, Visualization, Writing – original draft, Writing – review & editing. **André R. Niemeijer:** Conceptualization, Methodology, Validation, Supervision, Writing – review & editing. **Martyn R. Drury:** Writing – review & editing, Supervision, Methodology, Conceptualization. **Ernst Willingshofer:** Writing – review & editing, Supervision, Project administration, Methodology, Funding acquisition, Conceptualization. **Liviu C. Matenco:** Writing – review & editing, Supervision, Conceptualization.

Declaration of competing interest

The authors declare that they have no known competing financial interests or personal relationships that could have appeared to influence the work reported in this paper.

Data availability

All experimental mechanical data and microscopy images are available via YODA (data repository UU): DOI: 10.24416/UU01–9RRHVZ.

Supplementary materials

Supplementary material associated with this article can be found, in the online version, at doi:10.1016/j.epsl.2024.118586.

References

Bedford, J.D., Faulkner, D.R., Lapusta, N., 2022. Fault rock heterogeneity can produce fault weakness and reduce fault stability. Nat. Commun. 13 (1), 326. https://doi.org/10.1038/s41467-022-27998-2.

Beeler, N.M., Tullis, T.E., Blanpied, M.L., Weeks, J.D., 1996. Frictional behavior of large displacement experimental faults. J. Geophys. Res.: Solid Earth 101 (B4), 8697–8715. https://doi.org/10.1029/96JB00411.

Bourne, S.J., Oates, S.J., 2017. Extreme threshold failures within a heterogeneous elastic thin sheet and the spatial-temporal development of induced seismicity within the Groningen gas field. J. Geophys. Res.: Solid Earth 122 (12), 320. https://doi.org/10.1002/2017JB014356, 10,299-10.

Bourne, S.J., Oates, S.J., Bommer, J.J., Dost, B., van Elk, J., Doornhof, D., 2015. A Monte Carlo method for probabilistic hazard assessment of induced seismicity due to conventional natural gas production. Bull. Seismol. Soc. Am. 105 (3), 1721–1738. https://doi.org/10.1785/0120140302.

Buijze, L., 2020. Numerical and experimental simulation of fault reactivation and earthquake rupture applied to induced seismicity in the Groningen gas field. [Utrecht University]. https://doi.org/10.33540/60.

Buijze, L., Bogert, P.A.J., Wassing, B.B.T., Orlic, B., 2019. Nucleation and arrest of dynamic rupture induced by reservoir depletion. J. Geophys. Res.: Solid Earth 124 (4), 3620–3645. https://doi.org/10.1029/2018JB016941.

Buijze, L., Guo, Y., Niemeijer, A.R., Ma, S., Spiers, C.J., 2020. Effects of heterogeneous gouge segments on the slip behavior of experimental faults at dm scale. Earth and planetary sci. lett. 554, 116652 https://doi.org/10.1016/j.epsl.2020.116652.

Buijze, L., van den Bogert, P.A.J., Wassing, B.B.T., Orlic, B., ten Veen, J., 2017. Fault reactivation mechanisms and dynamic rupture modelling of depletion-induced seismic events in a Rotliegend gas reservoir. Neth. J. Geosci. 96 (5), s131–s148. https://doi.org/10.1017/njg.2017.27.

Byerlee, J. (1978). Friction of rocks. *Pure and Applied Geophysics, 116*(4), 615–626. https://doi.org/10.1007/BF00876528Byerlee, J., 1978. Friction of rocks 116, 12.

Caine, J.S., Evans, J.P., Forster, C.B., 1996. Fault zone architecture and permeability structure. Geology 24 (11), 1025. https://doi.org/10.1130/0091-7613(1996)024.

Chester, F.M., Chester, J.S., 1998. Ultracataclasite structure and friction processes of the punchbowl fault, San Andreas system, California. Tectonophysics 295 (1–2), 199–221. https://doi.org/10.1016/S0040-1951(98)00121-8.

Collettini, C., Niemeijer, A., Viti, C., Marone, C., 2009. Fault zone fabric and fault weakness. Nature 462 (7275), 907–910. https://doi.org/10.1038/nature08585.

Collettini, C., Tesei, T., Scuderi, M.M., Carpenter, B.M., Viti, C., 2019. Beyond byerlee friction, weak faults and implications for slip behavior. Earth Planet. Sci. Lett. 519, 245–263. https://doi.org/10.1016/j.epsl.2019.05.011.

Crawford, B.R., Faulkner, D.R., Rutter, E.H., 2008. Strength, porosity, and permeability development during hydrostatic and shear loading of synthetic quartz-clay fault gouge. J. Geophys. Res. 113 (B3), B03207. https://doi.org/10.1029/2006JB004634.

de Jager, J., Visser, C., 2017. Geology of the Groningen field – an overview. Neth. J. Geosci. 96 (5), s3–s15. https://doi.org/10.1017/njg.2017.22.

Dieterich, J.H., 1972. Time-dependent friction in rocks. J. Geophys. Res. 77 (20), 3690–3697. https://doi.org/10.1029/JB077i020p03690.

Dieterich, J.H., 1978. Preseismic fault slip and earthquake prediction. J. Geophys. Res. 83 (B8), 3940. https://doi.org/10.1029/JB083iB08p03940.

Dieterich, J.H., 1979. Modeling of rock friction: 1. experimental results and constitutive equations. J. Geophys. Res. 84 (B5), 2161. https://doi.org/10.1029/JB084iB05p02161.

Dieterich, J.H., 1981. Constitutive properties of faults with simulated gouge. In: Carter, N.L., Friedman, M., Logan, J.M., Stearns, D.W. (Eds.), Geophysical Monograph Series. American Geophysical Union, pp. 103–120. https://doi.org/10.1029/GM024p0103.

Dost, B., Ruigrok, E., Spetzler, J., 2017. Development of seismicity and probabilistic hazard assessment for the Groningen gas field. Neth. J. Geosci. 96 (5), s235–s245. https://doi.org/10.1017/njg.2017.20.

Dost, B., van Stiphout, A., Kühn, D., Kortekaas, M., Ruigrok, E., Heimann, S., 2020. Probabilistic moment tensor inversion for hydrocarbon-induced seismicity in the Groningen gas field, the Netherlands, part 2: application. Bull. Seismol. Soc. Am. 110 (5), 2112–2123. https://doi.org/10.1785/0120200076.

Fagereng, Å., Sibson, R.H., 2010. Mélange rheology and seismic style. Geology 38 (8), 751–754. https://doi.org/10.1130/G30868.1.

Faulkner, D.R., Jackson, C.A.L., Lunn, R.J., Schlische, R.W., Shipton, Z.K., Wibberley, C.A.J., Withjack, M.O., 2010. A review of recent developments concerning the structure, mechanics and fluid flow properties of fault zones. Journal of Structural Geology 32 (11), 1557–1575. https://doi.org/10.1016/j.jsg.2010.06.009.

Faulkner, D.R., Lewis, A.C., Rutter, E.H., 2003. On the internal structure and mechanics of large strike-slip fault zones: field observations of the carboneras fault in southeastern Spain. Tectonophysics. 367 (3–4), 235–251. https://doi.org/10.1016/S0040-1951(03)00134-3.

Faulkner, D.R., Sanchez-Roa, C., Boulton, C., den Hartog, S.A.M., 2018. Pore fluid pressure development in compacting fault gouge in theory, experiments, and nature. J. Geophys. Res.: Solid Earth 123 (1), 226–241. https://doi.org/10.1002/2017JB015130.

Giorgetti, C., Carpenter, B.M., & Collettini, C. (2015). *Frictional behavior of talc-calcite mixtures*. 120. https://doi.org/10.1002/2015JB011970.

Haines, S.H., Kaproth, B., Marone, C., Saffer, D., van der Pluijm, B., 2013. Shear zones in clay-rich fault gouge: A laboratory study of fabric development and evolution. Journal of Structural Geology 51, 206–225. https://doi.org/10.1016/j.jsg.2013.01.002.

Hunfeld, L.B., Niemeijer, A.R., Spiers, C.J., 2017. Frictional properties of simulated fault gouges from the seismogenic groningen gas field under in situ *p* - *T* -chemical conditions: friction of Groningen fault gouges. J. Geophys. Res.: Solid Earth 122 (11), 8969–8989. https://doi.org/10.1002/2017JB014876.

Ikari, M.J., Marone, C., Saffer, D.M., 2011. On the relation between fault strength and frictional stability. Geology 39 (1), 83–86. https://doi.org/10.1130/G31416.1.

Ikari, M.J., Saffer, D.M., Marone, C., 2009. Frictional and hydrologic properties of clay-rich fault gouge. J. Geophys. Res.: Solid Earth 114 (B5). https://doi.org/10.1029/2008JB006089.

Indraratna, B., Welideniya, H.S., Brown, E.T., 2005. A shear strength model for idealised infilled joints under constant normal stiffness. Géotechnique 55 (3), 215–226. https://doi.org/10.1680/geot.2005.55.3.215.

Knuth, M.W., Tobin, H.J., & Marone, C. (2013). Evolution of ultrasonic velocity and dynamic elastic moduli with shear strain in granular layers. Granular matter, 15(5), 499–515. https://doi.org/10.1007/s10035-013-0420-1.

Korkolis, E., Niemeijer, A.R., Paulssen, H., Trampert, J., 2021. A laboratory perspective on the gutenberg-richter and characteristic earthquake models. J. Geophys. Res.: Solid Earth (8), 126. https://doi.org/10.1029/2021JB021730.

Kortekaas, M., Jaarsma, B., 2017. Improved definition of faults in the Groningen field using seismic attributes. Neth. J. Geosci. 96 (5), s71–s85. https://doi.org/10.1017/njg.2017.24.

Leeman, J.R., Saffer, D.M., Scuderi, M.M., Marone, C., 2016. Laboratory observations of slow earthquakes and the spectrum of tectonic fault slip modes. Nat. Commun. 7 (1), 11104. https://doi.org/10.1038/ncomms11104.

Linker, M.F., Dieterich, J.H., 1992. Effects of variable normal stress on rock friction: observations and constitutive equations. J. Geophys. Res. 97, 4923–4940. https://doi.org/10.1029/92JB00017.

Logan, J.M., Friedman, M., Higgs, N., Dengo, C., Shimoto, T., 1979. Experimental studies of simulated gouge and their application to studies of natural fault zones. US Geol. Surv. Open-File Rep. 79–1239.

Marone, C., 1998. Laboratory-derived friction laws and their application to seismic faulting. Annu. Rev. Earth Planet Sci. 26 (1), 643–696. https://doi.org/10.1146/annurev.earth.26.1.643.

Moore, D.E., 2004. Crystallographic controls on the frictional behavior of dry and water-saturated sheet structure minerals. J. Geophys. Res. 109 (B3), B03401. https://doi.org/10.1029/2003JB002582.

Moore, D.E., Lockner, D.A., 2011. Frictional strengths of talc-serpentine and talc-quartz mixtures. J. Geophys. Res. 116 (B1), B01403. https://doi.org/10.1029/2010JB007881.

Niemeijer, A., C. Marone, and D. Elsworth (2010), Fabric induced weakness of tectonic faults, Geophys. Res. Lett., 37, L03304, doi:10.1029/2009GL041689.

Niemeijer, A.R., Collettini, C., 2013. Frictional properties of a low-angle normal fault under in situ conditions: thermally-activated velocity weakening. Pure Appl. Geophys. 171 (10), 2641–2664. https://doi.org/10.1007/s00024-013-0759-6.

Noël, C., Giorgetti, C., Scuderi, M.M., Collettini, C., Marone, C., 2023. The effect of shear displacement and wear on fault stability: laboratory constraints. J. Geophys. Res.: Solid Earth 128 (4), e2022JB026191. https://doi.org/10.1029/2022JB026191.

Ruina, A., 1983. Slip instability and state variable friction laws. J. Geophys. Res.: Solid Earth 88 (B12), 10359–10370. https://doi.org/10.1029/JB088iB12p10359.

Rutter, E.H., Hackston, A.J., Yeatman, E., Brodie, K.H., Mecklenburgh, J., May, S.E., 2013. Reduction of friction on geological faults by weak-phase smearing. J. Struct. Geol. 51, 52–60. https://doi.org/10.1016/j.jsg.2013.03.008.

Scholz, C.H., 2019. The Mechanics of Earthquakes and Faulting, 3rd ed. Cambridge University Press. https://doi.org/10.1017/9781316681473.

Scuderi, M.M., Collettini, C., Viti, C., Tinti, E., Marone, C., 2017. Evolution of shear fabric in granular fault gouge from stable sliding to stick slip and implications for fault slip mode. Geology. https://doi.org/10.1130/G39033.1. G39033.1.

Marone, C., Woods, S., Martell, R., & Leeman, J.R. (n.d.). Xlook. Available at: https://github.com/PennStateRockandSedimentMechanics/xlook.

Sibson, R.H. (1986). Earthquakes and rock deformation in crustal fault zones. 14, 149–175. https://doi.org/10.1146/annurev.ea.14.050186.001053.

Smeraglia, L., Billi, A., Carminati, E., Cavallo, A., Di Toro, G., Spagnuolo, E., Zorzi, F., 2017. Ultra-thin clay layers facilitate seismic slip in carbonate faults. Sci. Rep. 7 (1), 664. https://doi.org/10.1038/s41598-017-00717-4.

Smith, J.D., White, R.S., Avouac, J.-P., Bourne, S., 2020. Probabilistic earthquake locations of induced seismicity in the Groningen region, the netherlands. Geophys. J. Int. 222 (1), 507–516. https://doi.org/10.1093/gji/ggaa179.

Spetzler, J., Dost, B., 2017. Hypocenter estimation of induced earthquakes in Groningen. Geophys. J. Int. https://doi.org/10.1093/gji/ggx020 ggx020.

Tembe, S., Lockner, D.A., Wong, T.-F., 2010. Effect of clay content and mineralogy on frictional sliding behavior of simulated gouges: binary and ternary mixtures of quartz, illite, and montmorillonite. J. Geophys. Res. 115 (B3), B03416. https://doi.org/10.1029/2009JB006383.

Tesei, T., Collettini, C., Barchi, M.R., Carpenter, B.M., Di Stefano, G., 2014. Heterogeneous strength and fault zone complexity of carbonate-bearing thrusts with possible implications for seismicity. Earth Planet. Sci. Lett. 408, 307–318. https://doi.org/10.1016/j.epsl.2014.10.021.

Torabi, A., Ellingsen, T.S.S., Johannessen, M.U., Alaei, B., Rotevatn, A., Chiarella, D., 2020. Fault zone architecture and its scaling laws: where does the damage zone start and stop? Geolog. Society 496 (1), 99–124. https://doi.org/10.1144/SP496-2018-151.

Van Ojik, K., Böhm, A., Cremer, H., Geluk, M., De Jong, M., Mijnlieff, H., Nio, S.D., 2012. The rationale for an integrated stratigraphic framework of the upper rotliegend ii depositional system in the Netherlands. The Permian Rotliegend of the Netherlands. SEPM (Society for Sedimentary Geology), pp. 37–48. https://doi.org/10.2110/pec.11.98.0037 (Special Publication).

van Thienen-Visser, K., & Breunese, J.N. (2015). Induced seismicity of the Groningen gas field: history and recent developments. The leading edge, 34(6), 664–671. https://doi.org/10.1190/tle34060664.1.

Van Wees, J.-D., Fokker, P.A., Van Thienen-Visser, K., Wassing, B.B.T., Osinga, S., Orlic, B., Ghouri, S.A., Buijze, L., Pluymaekers, M, 2017. Geomechanical models for induced seismicity in the Netherlands: inferences from simplified analytical, finite element and rupture model approaches. Neth. J. Geosci. 96 (5), s183–s202. https://doi.org/10.1017/njg.2017.38.

Vrolijk, P.J., Urai, J.L., Kettermann, M., 2016. Clay smear: review of mechanisms and applications. J. Struct. Geol. 86, 95–152. https://doi.org/10.1016/j.jsg.2015.09.006.

Willacy, C., van Dedem, E., Minisini, S., Li, J., Blokland, J.-W., Das, I., Droujinine, A., 2019. Full-waveform event location and moment tensor inversion for induced seismicity. Geophysics 84 (2), KS39–KS57. https://doi.org/10.1190/geo2018-0212.1.